

Transport properties of finite- β microturbulence

M. J. Pueschel^{1,2} and F. Jenko¹

¹Max-Planck-Institut für Plasmaphysik, EURATOM Association, D-85748 Garching, Germany

²Max-Planck-Institut für Sonnensystemforschung, D-37191 Katlenburg-Lindau, Germany

(Received 11 February 2010; accepted 5 May 2010; published online 22 June 2010)

Via nonlinear gyrokinetic simulations, microturbulent transport is investigated for electromagnetic trapped electron mode (TEM) and ion temperature gradient (ITG) tokamak core turbulence with β up to and beyond the kinetic ballooning mode threshold. Deviations from linear expectations are explained by zonal flow activity in the TEM case. For the ITG scenario, β -induced changes are observed in the nonlinear critical gradient upshift—from a certain β , a strong increase is observed in the Dimits shift. Additionally, a Rechester–Rosenbluth-type model for magnetic transport is applied, and the amplitudes of magnetic field fluctuations are quantified for different types of turbulence. © 2010 American Institute of Physics. [doi:10.1063/1.3435280]

I. INTRODUCTION

Finite plasma β and the associated electromagnetic effects can have a significant influence on the quality of confinement in fusion experiments. To date, it is poorly understood why different machines and discharges display apparently inconsistent scalings, some of which are rather unfavorable.^{1,2} Additionally, the parameter governs the bootstrap fraction as well as the fusion reaction rate and imposes limits on operation regimes. Therefore, and in light of the fact that experimentally, no clear quantitative understanding of the impact of β on the confinement exists, numerical investigations of the matter are of great importance.

Electromagnetic core microturbulence has been studied by means of both gyrokinetic^{3–7} and gyrofluid^{8–11} simulations. Few nonlinear results, however, have been reported for (higher) β values near and at the kinetic ballooning mode (KBM) threshold. Both current and future fusion devices require the highest feasible β to operate at maximum efficiency. It is thus paramount to have a precise understanding of the nonlinear behavior of the transport near the KBM critical β .

Recently, advances have been made in extending the achievable β range of nonlinear gyrokinetic simulations and explaining the observed turbulent transport.^{7,12} More specifically, a significant reduction in transport levels was observed which could not be explained by the linear physics alone, including by a standard quasilinear model.^{13,14} The present work aims to both extend and generalize these findings by examining both linear and nonlinear gyrokinetic simulations in the ion temperature gradient (ITG) and the trapped electron mode (TEM) regime, in addition to the runs published in Ref. 7 which employed cyclone base case¹⁵ (CBC) parameters.

This paper is organized as follows. First, a brief overview of the gyrokinetic code GENE is given which was used to obtain the results presented here. In the following two sections, parameters, simulation results, and analyses of the TEM and ITG case β scans are presented, with an emphasis on explaining the deviations of the turbulent transport levels

from the linear expectations. Comparisons with the CBC scan are made to generalize certain findings. Next, the focus shifts to the magnetic properties of the aforementioned simulations: a model for magnetic transport is verified, and coefficients describing the amplitude of the magnetic fluctuations are provided. Lastly, the findings from the above sections are summarized and the paper is concluded.

II. GENE SIMULATIONS

All simulations in the context of this work were performed with the nonlinear gyrokinetic Vlasov code GENE.^{16–20} The GENE code solves the gyrokinetic Vlasov equation alongside Maxwell's equations, treating the electrostatic and electromagnetic potentials, Φ and $(A_{\parallel}, B_{\parallel})$, respectively, self-consistently. To reduce the computational requirements, field aligned coordinates are used: x serves as a flux surface label, z as the (poloidal) coordinate along the field line, and y denotes the remaining third direction. The velocity space is spanned by the parallel velocity v_{\parallel} and the magnetic moment μ .

Note that for $\beta \ll 1$, parallel magnetic fluctuations B_{\parallel} are small, and are thus neglected here. By convention, the (electron) plasma pressure β is defined to be

$$\beta \equiv \beta_e = \frac{8\pi n_e T_e}{B_{\text{ref}}^2} \quad (1)$$

for the remainder of this paper. When operating in its linear mode, the code has an eigenvalue solver complementing its initial value solver, making subdominant and stable modes accessible.²¹

Although all simulations presented here were performed in local \hat{s} - α flux tube geometry (with $\alpha \equiv \alpha_{\text{MHD}}$ set to zero) to allow for convenient comparison with other codes (as was done in Ref. 7), GENE is able to utilize general, experimental equilibria,²² and may also be run in its radially nonlocal mode. In the following sections, results from GENE simulations are reported and analyzed, starting with an investigation into TEM turbulence.

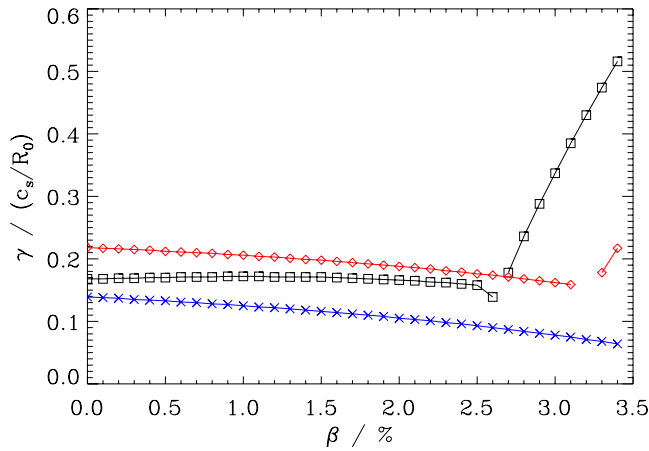


FIG. 1. (Color online) Linear growth rates for the TEM β scan. Shown are the results for $k_y \rho_s = 0.2$ (black squares), 0.4 (red diamonds), and 0.6 (blue crosses). At higher β values, the TEM growth rates are exceeded by that of the KBMs.

III. TEM TURBULENCE

TEMs are known to occur on scales similar to ITG modes and may contribute to the observed anomalous transport. Recently, advances have been made in explaining the saturation mechanisms of TEM turbulence.^{23–25} In this section, the effects of finite β on both linear and nonlinear TEMs are to be examined.

A. Physical and numerical parameters

TEMs may be classified as either temperature gradient driven or density gradient driven, depending on the gradient settings and the critical gradients of the physical scenario.²⁶ This section focuses on a case somewhat in between: in order to avoid a smooth transition from the TEM to an ETG mode at large k_y which may complicate the interpretation of nonlinear simulation results, the electron temperature gradient is chosen relatively low and the density gradient moderately high. The corresponding parameter choice is

$$\omega_{Ti} = 2, \quad \omega_{Te} = 4, \quad \omega_n = 3, \quad \hat{s} = 0.796,$$

$$q_0 = 1.4, \quad \epsilon_r = 0.18, \quad T_i/T_e = 1,$$

where $\omega_{Tj} = R_0/L_{Tj}$ is the normalized temperature gradient of species j , with R_0 being the major radius, $\omega_n = R_0/L_n$ is the normalized density gradient, \hat{s} is the magnetic shear, q_0 is the safety factor, $\epsilon_r = r_0/R_0$ is the inverse aspect ratio, and T_j is the equilibrium temperature of species j . Both ions and electrons are treated kinetically, with a mass ratio of $m_i/m_e = 1836$. Note that the gradient choice results in $\eta_e = \omega_{Te}/\omega_n \sim 1$, corresponding to a typical threshold between density gradient and temperature gradient driven TEMs.

The numerical settings were chosen as follows. In the linear simulations, the parallel coordinate is resolved by 24 points, and five radial connections are retained (corresponding to 11 complex radial modes). 48 points span the parallel velocity space, while the magnetic moment coordinate has 16 points. GENE also employs hyperdiffusion^{19,27} to suppress the occurrence of unphysical modes which are excited due to

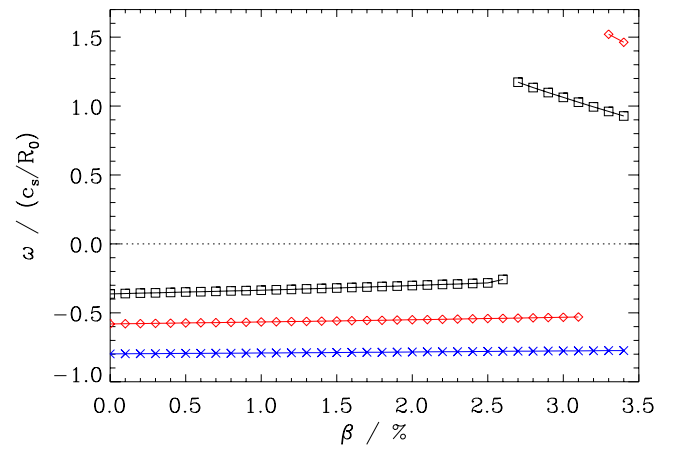


FIG. 2. (Color online) Real frequencies for the TEM β scan. Shown are the results for $k_y \rho_s = 0.2$ (black squares), 0.4 (red diamonds), and 0.6 (blue crosses). At higher β values, KBMs become the dominant instability.

properties of centered differencing stencils. The settings for the parallel hyperdiffusion coefficient is $\epsilon_z = 4$, which acts on the Vlasov equation via the hyperdiffusion term

$$D_4 = -\epsilon_z \left(\frac{\Delta z}{2} \right)^4 \nabla_{\parallel}^4. \quad (2)$$

It should be noted that the simulations show very little sensitivity to this value.

For nonlinear runs, a perpendicular box of $125.6\rho_s \times 125.7\rho_s$ is resolved by 192×24 (complex) Fourier modes, corresponding to 192×48 spatial grid points in the x and y coordinates, respectively. For the nonlinear run at $\beta = 2.1\%$, an increased box size of $251.3\rho_s \times 150.8\rho_s$ was chosen (resolved by 48 binormal Fourier modes) to prevent radial structures from self-connecting via the radial (periodic) boundary condition. Note that the perpendicular normalization length is $\rho_s = c_s/\Omega_i$, with the ion gyrofrequency Ω_i and $c_s = (T_e/m_i)^{1/2}$, while time scales are specified in units of c_s/R_0 . The parallel resolution is increased by a factor of 2 while the magnetic moment space is spanned by eight grid points. ϵ_z is set to 12. Convergence was tested successfully both linearly and nonlinearly in all spatial and velocity space dimensions, as well as with respect to the parallel hyperdiffusivity. This was done separately in the electrostatic limit and at a moderate β value of 1%, with deviations of $\lesssim 10\%$.

B. Linear results

For $k_y \rho_s$ from 0.2 to 0.6 and a range of β values, the linear growth rate γ and the (real) frequency ω are shown in Figs. 1 and 2, respectively. Conforming with the general expectations, e.g., in Ref. 7, the linear TEM is subjected to very little modification as β increases. At $\beta = \beta_{\text{crit}}(k_y \rho_s = 0.2) = 2.7\%$, a KBM takes over at $k_y \rho_s = 0.2$, its growth rate increasing rapidly, whereas a discontinuity in the frequency is observed. For higher k_y , the critical value rises quickly. Figure 3 shows the critical β for a larger range of k_y . As is to be expected, the magnetohydrodynamics (MHD) limit $\beta_{\text{crit}}^{\text{MHD}} = 2.03\%$ – here, a simple estimate $\alpha_{\text{MHD}}^{\text{crit}} = 0.6\hat{s}$ was used, but taking the more precise MHD value²⁸ yields no

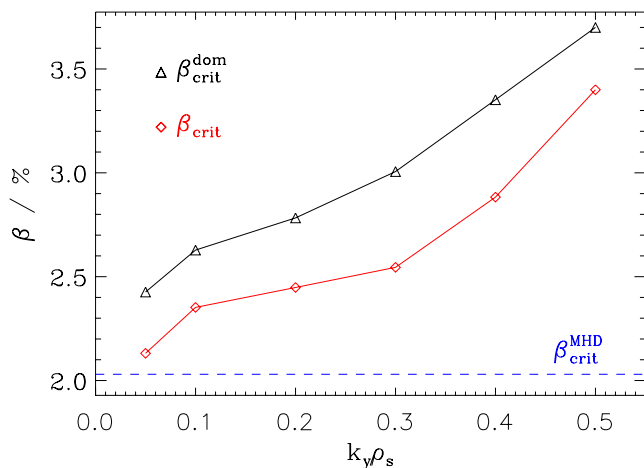


FIG. 3. (Color online) Spectra of the KBM critical β values. Black triangles denote the β where the KBM becomes the dominant instability, whereas red diamonds correspond to the point of marginal KBM stability (see the text). For reference, the MHD estimate is shown as a blue dashed line.

significantly different result – is retained for $k_y \rightarrow 0$, and the KBM appears first at the smallest simulated k_y . Note that in the figure, $\beta_{\text{crit}}^{\text{dom}}$ is the point where the KBM growth rate starts to exceed that of the TEM, while at β_{crit} , the KBM is marginally stable and subdominant. For more details, see Ref. 7. Note that the overall kinetic threshold is determined by the threshold at that k_y where the KBM is destabilized first,

$$\beta_{\text{crit}} \equiv \min_{k_y} \beta_{\text{crit}}(k_y) \approx \beta_{\text{crit}}^{\text{MHD}}, \quad (3)$$

which, in the present case, coincides with the MHD threshold—not surprisingly, since the MHD result has to be retained as $k_y \rightarrow 0$.

Next, results from a nonlinear investigation will be presented to establish whether the slowly declining growth rate carries over qualitatively. In addition, the question will have to be answered whether the linear and nonlinear KBM thresholds coincide, as likely, the transport spectra will not peak at the k_y with the lowest β_{crit} , i.e., the lowest k_y .

C. Nonlinear transport

Transport levels obtained from nonlinear simulations are reported in Fig. 4. Here, the TEM behaves somewhat differently compared with the linear case: unlike the near-constant, slightly declining growth rate, the dominant electrostatic heat flux Q_e^{es} grows slowly with increasing β . The same is true for the ion heat flux Q_i^{es} , as well as for the particle flux Γ^{es} . Stronger growth is observed for the electron magnetic heat flux Q_e^{em} —as detailed in Ref. 7, magnetic fluxes comparable with the electrostatic fluxes are also observed at CBC parameters. Further below, a more detailed analysis of the magnetic transport will be provided.

Exemplarily, the time evolution of the most important heat fluxes for the simulation at $\beta=1.5\%$ is shown in Fig. 5. The nonlinearly saturated phase is reached after a few ten time units.

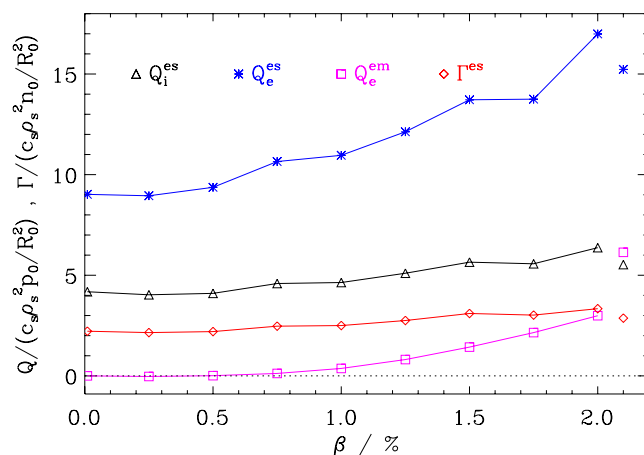


FIG. 4. (Color online) Nonlinear heat and particle fluxes for the TEM case β scan. Black triangles denote the ion electrostatic heat flux, blue stars the electron electrostatic heat flux, and pink squares the electron electromagnetic heat flux. The electrostatic particle flux is shown as red diamonds. The other transport channels are small in comparison with those included in this figure. For $\beta \leq 2\%$, the turbulence has a clear TEM character, whereas at $\beta=2.1\%$, both TEM and KBM characteristics may be found.

At $\beta=2.1\%$, some qualitative changes occur (prompting a larger perpendicular box size to ensure convergence). Most significantly, small KBM contributions start to appear in the nonlinear frequencies. Typically, such behavior is caused by one or more subdominant linear instabilities competing with the dominant mode nonlinearly, resulting in a dip of the transport channels.¹⁸ In Ref. 7, such mode interactions have been observed for the CBC, while in the present TEM case, they explain the slightly lower transport at $\beta=2.1\%$. It thus follows that $\beta_{\text{crit}}^{\text{nonlin}} \approx 2.1\%$, nearly identical to the linear threshold.

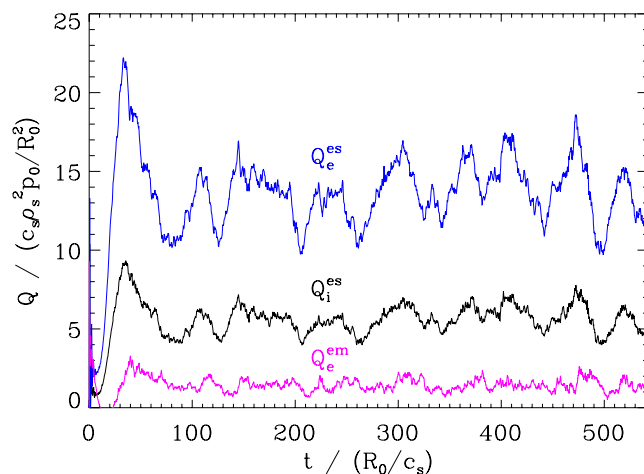


FIG. 5. (Color online) Nonlinear heat fluxes for the TEM simulation at $\beta=1.5\%$ as a function of time. From top to bottom, the quantities shown here are the electron electrostatic heat flux Q_e^{es} (blue), its ion counterpart Q_i^{es} (black), and the electron electromagnetic heat flux Q_e^{em} (pink). After an initial linear phase, nonlinear saturation is achieved in all channels.

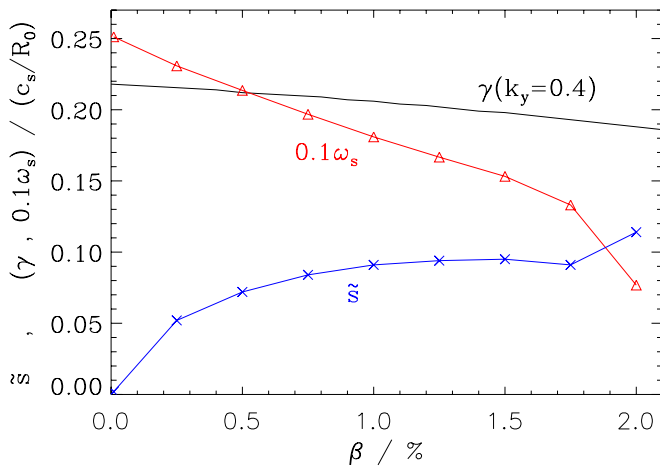


FIG. 6. (Color online) Shearing rate (red triangles, rescaled) and shear fluctuations (blue crosses) for the TEM case. While it is declining more quickly than the growth rate (shown here for the dominant $k_y\rho_s=0.4$, black line), the shearing rate is larger by roughly an order of magnitude throughout the TEM regime. In contrast, the shear fluctuations always remain much smaller than the equilibrium shear $\hat{s}=0.796$.

D. Zonal flow activity

Although TEM turbulence is known to often exhibit streamer activity, zonal flows may also have an influence on transport levels to the point where they may become the primary saturation mechanism (see, e.g., Refs. 26 and 24). In the electrostatic potential, these structures have constant amplitudes on flux surfaces and may perturb or even destroy radial streamers, thereby depriving the plasma of an effective transport mechanism and thus lowering the radial transport levels. More quantitatively, it has recently been found²⁵ for the electrostatic case that for $\omega_{Te}/\omega_n \lesssim 1$, zonal flows can indeed significantly influence TEMs. As $\omega_{Te}/\omega_n \approx 1.3$ in the present case, the operation point is rather close to this limit. Additionally, the ion temperature gradient is set to a finite value (unlike in Ref. 25), and finite- β effects may change the zonal flow dynamics.

A quantitative measure of the zonal flow strength is the (normalized) shearing rate,

$$\omega_s = \frac{d^2\Phi_{\text{zon}}}{dx^2}. \quad (4)$$

Here, Φ_{zon} is the zonal component of the electrostatic potential. Motivated by finite-frequency corrections,²⁹ a simple yet reasonably general condition for zonal flows to have an impact on nonlinear saturation is met when the shearing rate exceeds the dominant linear growth rate (here at $k_y\rho_s=0.4$) by about an order of magnitude,³⁰ $\omega_s \gtrsim 10\gamma$.

Figure 6 shows the (rescaled) shearing rate as a function of the plasma β , with the linear growth rate at $k_y\rho_s=0.4$ also shown for comparison. Clearly, the shearing rate declines much faster than γ , indicating that as β gets larger, the zonal flow activity becomes less important. When comparing this finding with the (electrostatic) transport curves, it can be conjectured that as β is increased, the heat transport is less inhibited by the zonal flows.

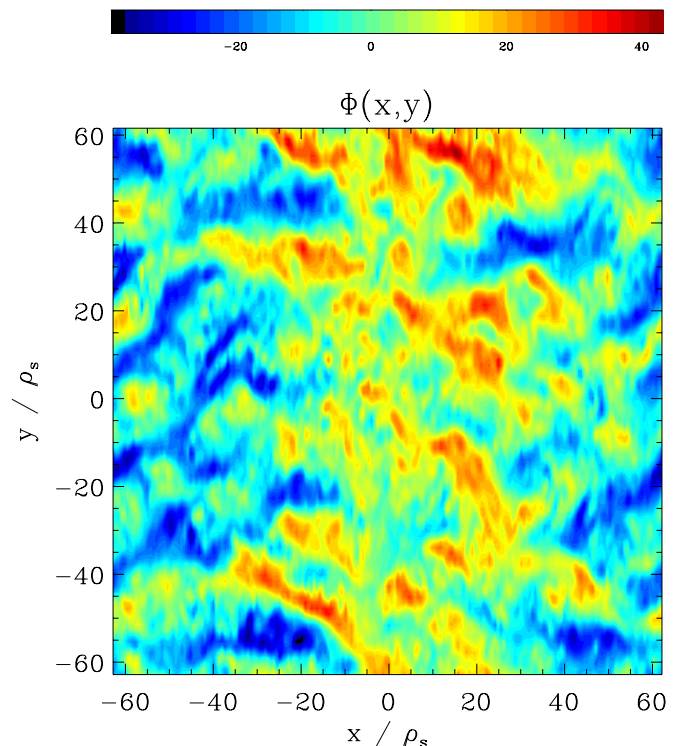


FIG. 7. (Color online) Contours of the electrostatic potential for the TEM case in the electrostatic limit ($\beta=0.01\%$) during the saturated phase. A weak zonal flow can be seen to comprise a number of small, streamerlike structures.

In order to put this finding on more solid footing, runs were performed where the zonal component of the field was zeroed out. For the electrostatic case, this caused the transport to increase by a few 10% while for $\beta=1.5\%$, the increase was only half as strong, indicating that the impact of zonal flows is stronger for lower β values, which is in line with the shearing rate behavior and its above interpretation.

As TEM turbulence tends to exhibit streamerlike features, it is not surprising that zonal flows are not dominantly visible in the x - y plane, as can be seen in Figs. 7 and 8 which show contours of the electrostatic potential for $\beta=0.01\%$ and 1.75% , respectively. In the former plot, small streamerlike structures form a weak zonal flow—in the latter, however, the zonal flow has clearly broken up. This is in line with the aforementioned statement that zonal flow activity is reduced for higher β .

It is to be noted that this investigation may be thought of as an extension of parameter space of the (electrostatic) work published in Refs. 26 and 24 where zonal flows in TEM turbulence were regulated via adjustments in the gradients. As a high β diminishes zonal flows, it can be conjectured that the parameter space where TEM turbulence is affected by zonal flows may shrink with respect to simple electrostatic expectations.

Lastly, the shear fluctuation caused by magnetic perturbations is also included in Fig. 6,

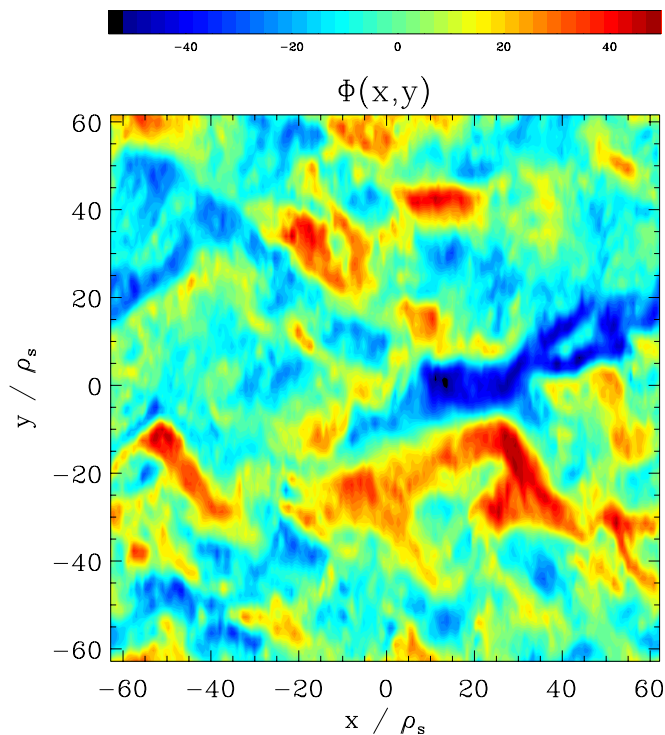


FIG. 8. (Color online) Contours of the electrostatic potential for the TEM case at $\beta=1.75\%$. In this β range, the zonal flow activity which was present at lower β has become all but negligible, which is reflected by the absence of vertical structures in this plot.

$$\tilde{s} = q_0 \frac{R_0}{B_{\text{ref}}} \frac{dB_y}{dx}. \quad (5)$$

As their magnitude always remains significantly smaller than the equilibrium shear $\hat{s}=0.796$, no significant influence is to be expected (see also Ref. 7).

In the present case of TEM turbulence, it was found that the linear and nonlinear simulations exhibited qualitatively different behavior, which was explained by β -induced modifications to the zonal flow dynamics. The ballooning threshold, on the other hand, agrees well between linear simulations, nonlinear simulations, and the MHD value. Below, an ITG scenario will be studied to see whether the above findings can be applied to a different type of turbulence, as well.

IV. ITG TURBULENCE

A. Physical and numerical parameters

In Ref. 7, ITG turbulence was investigated at CBC parameters where mode interactions of ITG modes with TEMs made it difficult to quantify the influence of different transport-reducing mechanisms. To isolate ITG turbulence features from those of other microturbulence types, an ITG operation point different from that of the CBC was selected for the simulations presented in this section.

To this end, the gradients were adjusted from the TEM case to

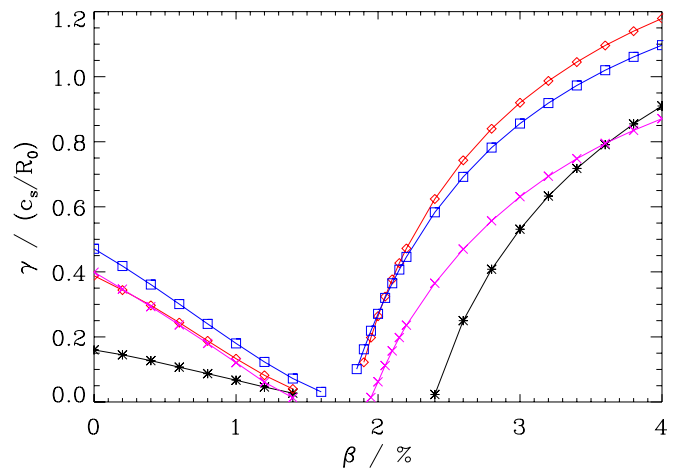


FIG. 9. (Color online) Linear growth rates for the ITG scenario β scan. Displayed are $k_y \rho_s = 0.1$ (black stars), 0.2 (red diamonds), 0.3 (blue squares), and 0.4 (pink crosses). The left part of the plot exhibits dominant ITG modes up until they are stabilized by the increasing β . After crossing the corresponding threshold, a KBM grows quickly.

$$\omega_{Ti} = 8, \quad \omega_{Te} = 0, \quad \omega_n = 1,$$

leaving only ITG modes (and KBMs at higher β) unstable. All other physical parameters were left identical to those of the TEM case. The parallel hyperdiffusion coefficient was set to $\epsilon_z = 8$ for both linear and nonlinear runs. Again, checks were performed linearly and nonlinearly which determined convergence in all coordinates and the parallel hyperdiffusivity electrostatically and at $\beta=0.5\%$. Since throughout a significant β range, very little transport is observed, it is difficult to identify a good point for testing convergence—while at 0.5%, there is still some transport remaining, a sometimes burstlike nature of the respective simulations was observed, making it harder to obtain good statistics. Therefore, convergence was achieved to only $\leq 20\%$ in some cases due to bursts ($\leq 10\%$ for the electrostatic tests).

B. Linear results

The linear growth rates and frequencies (see Figs. 9 and 10, respectively) follow the general expectations: the ITG mode is getting weaker as β is increased; there is a small gap where, essentially, no instability occurs; and at a critical β , the KBM starts to grow, accompanied by a jump in the frequency.

Much like in the CBC, the KBMs set in first at around $k_y \rho_s = 0.2-0.3$ (see Fig. 11), coinciding with the spectral maximum of both the growth rate and the nonlinear transport. Note that $\beta_{\text{crit}} = 1.8\%$, while $\beta_{\text{crit}}^{\text{MHD}} = 2.44\%$ —KBM s may be excited at significantly lower β than one may expect from the MHD prediction. This finding also agrees with the CBC data qualitatively, while here, the reduction is even stronger at $\sim 26\%$, highlighting the necessity of performing at least linear simulations to determine β_{crit} rather than relying on the MHD estimate.

Generally, one is to expect such behavior in the presence of an ion temperature gradient³¹ which for the ITG case is

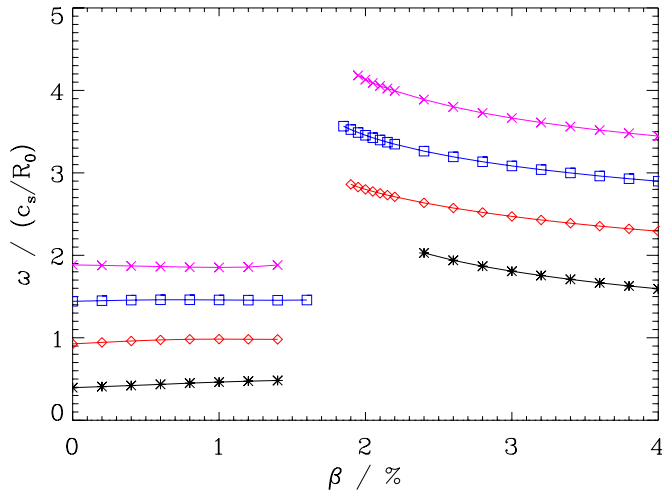


FIG. 10. (Color online) Linear frequencies for the ITG scenario β scan. Displayed are $k_y \rho_s = 0.1$ (black stars), 0.2 (red diamonds), 0.3 (blue squares), and 0.4 (pink crosses). In the lower half of the β range, a clear ITG signature is found, while in the higher half, typical KBM frequencies appear.

even higher than in the CBC. On the other hand, it will remain to be seen whether the KBM threshold is also lowered that much nonlinearly, as will be determined below.

C. Nonlinear transport

In Fig. 12, nonlinear transport levels are shown for the ITG case. Q_i^{es} displays behavior qualitatively similar to that of the linear growth rate γ . For the declining ITG branch, however, the slope of γ is much steeper, suggesting that much like in the CBC, nonlinear processes inhibit radial heat transfer. Since ω_{Ti} dominates the other gradients, the relative contributions of Q_e^{es} and Γ^{es} are small. In particular, due to $\omega_{Te} = 0$, the electron magnetic transport Q_e^{em} is negligible over most of the β range and only starts to grow once the KBM threshold is crossed at $\beta_{crit}^{nonlin} = 1.9\%$, at which point even its ion counterpart Q_i^{em} becomes non-negligible, but with opposite sign, more than canceling out the impact of the

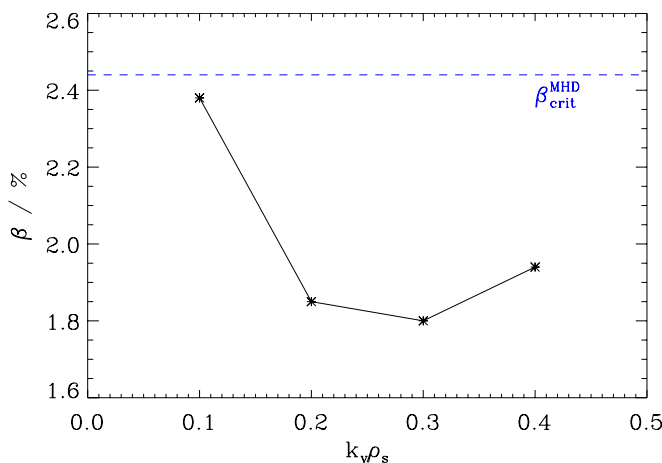


FIG. 11. (Color online) Spectra of the KBM critical β values (black stars). Note that in the current ITG scenario, β_{crit} and β_{crit}^{dom} are identical by definition. For reference, the MHD estimate is shown as a blue dashed line.

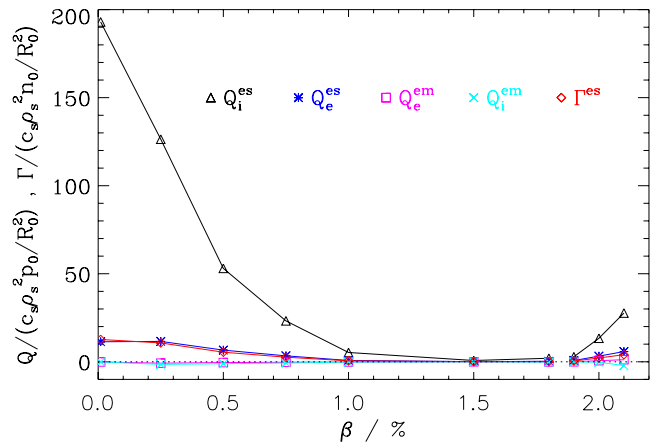


FIG. 12. (Color online) Transport levels for the ITG case β scan. Black triangles denote the ion, blue stars the electron electrostatic heat flux; pink squares the electron and cyan crosses the ion electromagnetic heat flux; and red diamonds the electrostatic particle flux. From $\beta = 1.9\%$, the turbulence is of KBM type.

former. Note that low magnetic transport does not necessarily correspond to a small magnetic fluctuation level, as shall be discussed later.

Again, the time evolution of the dominant heat fluxes for the simulation at $\beta = 1.5\%$ is shown exemplarily, see Fig. 13. At this β , the ITG turbulence is essentially stabilized, leading to the quiescent behavior observed here.

The nonlinear KBM threshold agrees well with the linear kinetic value $\beta_{crit} = 1.8\%$. Since this finding applies to all cases investigated so far – CBC, TEM, ITG – it is concluded that the linear and nonlinear KBM thresholds are the same and that linear studies are thus sufficient to obtain KBM (in)stability regimes. In contrast, β_{crit}^{MHD} , while useful as an initial estimate, is too imprecise and may easily predict KBM stability where the actual threshold has already been crossed.

As mentioned above, nonlinear mode interaction cannot cause the phenomenon of strongly declining transport in the present case, as no additional linearly unstable modes were

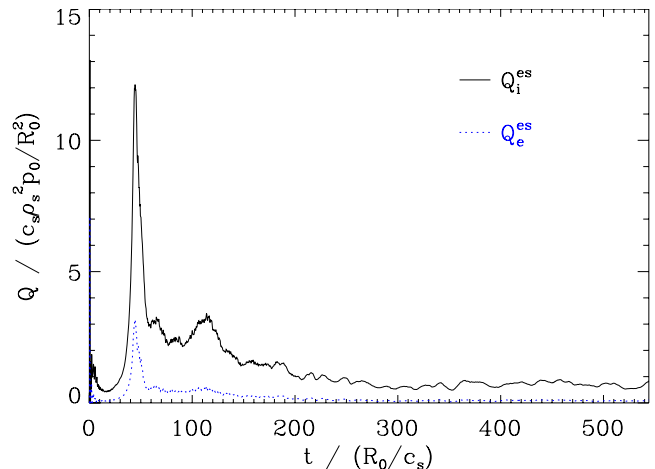


FIG. 13. (Color online) Nonlinear heat fluxes for the ITG simulation at $\beta = 1.5\%$ as a function of time. The ion electrostatic heat flux Q_i^{es} is denoted by a solid black line, its electron counterpart Q_e^{es} by a dotted blue line. After an initial linear phase, nonlinear saturation is achieved.

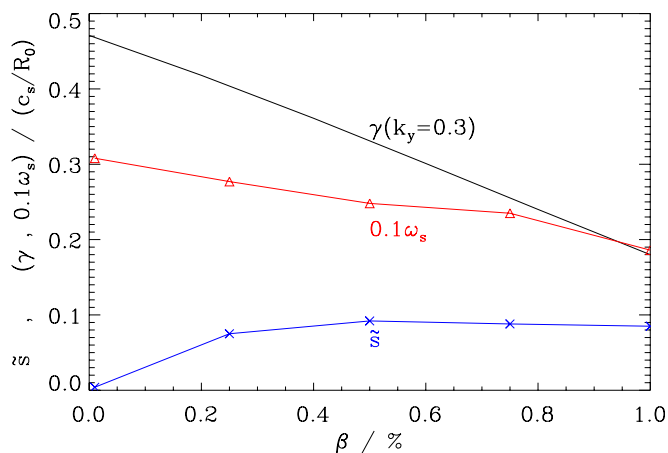


FIG. 14. (Color online) Shearing rate (red triangles, rescaled) and shear fluctuations (blue crosses) for the ITG case. The growth rate (shown here for the dominant $k_y \rho_s = 0.3$, black line) is declining more rapidly than the shearing rate, while the latter is larger by roughly an order of magnitude, causing zonal flows to gain in influence with increasing β . As in the TEM case, the shear fluctuations always remain much smaller than the equilibrium shear.

found which may have been able to compete with the dominant ITG mode. Thus, a different explanation is required, again prompting a look at zonal flows: Fig. 14 shows the (rescaled) shearing rate along with the linear growth rate at $k_y \rho_s = 0.3$. The former is found to decline much more slowly than the growth rate. Thus, with $\omega_s \approx 10\gamma$ and ω_s/γ increasing with β , zonal flows become more important for larger values of β . From the data at hand, however, it cannot be concluded whether this alone is sufficient to explain the sharp drop in the nonlinear transport.

Interestingly, just as in the TEM case, the zonal flow strength (as quantified, e.g., by the shearing rate) decreases slowly with β . As is described, e.g., in Ref. 32, the (electrostatic) Reynolds stress – which tends to be largely responsible for the nonlinear generation of zonal flows – can be (partially) offset for larger β values by the (electromagnetic) Maxwell stress. At the same time, the Reynolds stress itself may simply be reduced with increasing β . For gyrofluid simulations of edge turbulence,^{33,34} both of these trends have been reported. Although no such measurements were performed here, the aforementioned findings regarding the transport behavior of core ITG or TEM turbulence qualitatively agree with such scenarios.

Regarding nonlinear ITG runs, a current discussion about nonlinear simulations at $\beta \lesssim \beta_{\text{crit}}$ is focusing on why it is fairly hard to achieve saturation at CBC parameters. For that case, it has been shown that several codes agree on a runaway β value above which saturation is not achieved³⁵ for a wide range of initial conditions (including the standard initial conditions employed in the present work). The runaway β threshold, however, does not coincide with the nonlinear KBM threshold. Instead, the latter agrees very well with the linear critical β .⁷ To preclude any confusion, it is to be noted that hyperdiffusion has no impact on the runaway phenomenon. Techniques or adjustments to avoid transport runaway, like using initial conditions close to the expected saturated regime – e.g., by continuing a low- β run at higher

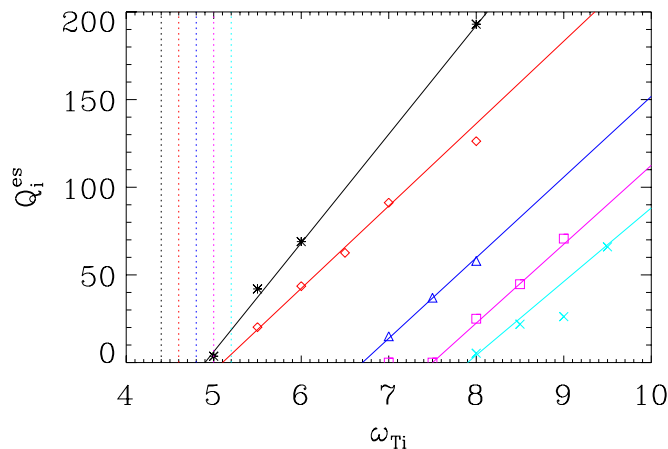


FIG. 15. (Color online) Critical gradient study for the ITG case β scan. As functions of the ion temperature gradient, the electrostatic ion heat flux is plotted for different values of β : 0.01% (black stars), 0.25% (red diamonds), 0.5% (blue triangles), 0.75% (pink squares), and 1.0% (cyan crosses; the outlier was excluded for the fit). The linear critical gradients for these β values are included for reference as dotted vertical lines (the order from left to right is the same as that of the above (ascending) β values). Most notably, a significant gap exists between the $\beta = 0.25\%$ and 0.5% nonlinear critical gradients.

β – were used in Ref. 7 but were not required for any of the simulations performed in the context of the present work.

In the present work, the parameter regimes are sufficiently different from the CBC that no such sub- β_{crit} runaway phenomena were observed—with the exception of runaway transport at large times (i.e., after a reasonably long saturated regime, unlike the runaways observed for CBC parameters) for the single point at highest β and ω_{Ti} in Fig. 15. Only when the KBM threshold was crossed did saturation become difficult. The results presented above may be used to rule out or possibly substantiate certain theories as to where the runaway phenomenon may originate from.

D. β -modified critical gradient upshift

In order to understand the transport reduction, an analysis of both the linear and the nonlinear critical temperature gradients was performed. It is well established that there exists an upshift of the critical ion temperature gradient when going from linear to nonlinear ITG simulations, the so-called Dimits shift.¹⁵ Recently, the Dimits shift was found to be fairly robust in simulations with realistic geometries which also included finite- β effects.³⁶ However, no systematic study exists as to how the critical gradient upshift may change when β is varied.

In Fig. 15, the results of a corresponding study are shown, and the nonlinear critical gradients are obtained. Those, along with their linear counterparts, are plotted in Fig. 16 as functions of β . In the linear case, only a small, linear increase is observed over the displayed β range. This increase goes hand in hand with the growth rate reduction with increasing plasma β . Comparing these data with the nonlinear results, however, one finds significant differences. Where $\omega_{Ti, \text{crit}}^{\text{lin}}$ increases only by about 14%, the increase becomes 61% for the nonlinear $\omega_{Ti, \text{crit}}^{\text{nonlin}}$. The resulting upshift is thus amplified by a factor of 5.4 compared with the electro-

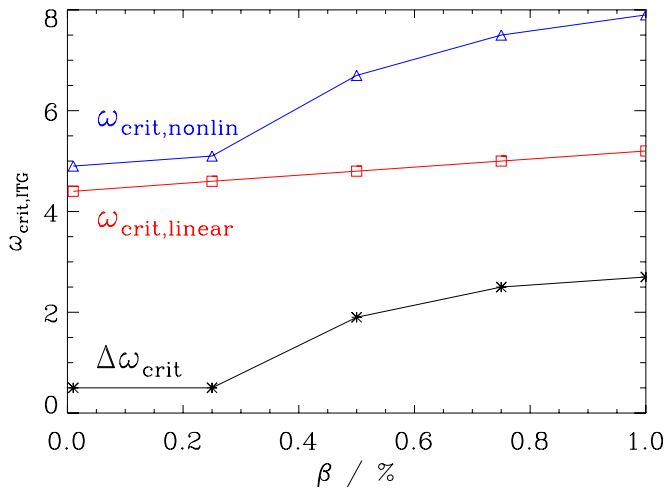


FIG. 16. (Color online) The critical ion temperature gradients are plotted for the linear (red squares) and the nonlinear (blue triangles) case as functions of β , as is the difference between those quantities (black stars). The initially small difference grows to reach values >2 , radically enlarging the Dimits shift.

static limit. As both standard and additional diagnostics revealed no qualitative changes or significant jumps in this β range, the sudden and rather drastic increase in $\omega_{Ti,crit}^{nonlin}$ when going from $\beta=0.25\%$ to 0.5% is unexpected—the only connection to other data that were observed is its link with the steeper-than-linear decline of the transport with β .

It should be emphasized that while measurements of the nonlinear critical gradient are prone to significant uncertainties – mostly due to burstlike phenomena in and near the Dimits regime that can make it difficult to obtain meaningful statistics of time-resolved data – the results presented here leave no doubt that a radically increased upshift occurs at high β . The precise functional dependence of this upshift on the plasma pressure, however, cannot be deduced from the data at hand. Note that in the present case, nonlinear ITG stabilization via increasing β leads to complete suppression of microturbulence, whereas in the CBC scenario, once the ITG level reaches that of the TEM, the latter takes over.

Defining the slope $\alpha_{\Delta\omega} = \partial Q_i^{es} / \partial \omega_{Ti}$ of the gradient-resolved transport curves shown in Fig. 15, one obtains $\alpha_{\Delta\omega} \sim 60$ for the electrostatic limit and $\alpha_{\Delta\omega} \sim 45$ for all other β values. Consequently, there is little change with regard to how sensitive to small gradient adjustments the system is when near the critical gradient. In other words, β has only a rather small effect on the profile stiffness for the present scenario.

After this investigation of the influence of β on primarily the electrostatic transport channels, the next section focuses on the magnetic flutter transport of electrons due to field line perturbations.

V. VERIFYING A MODEL FOR THE MAGNETIC TRANSPORT

The heat flux of the electrons caused by their motion along radially perturbed field lines is predicted well by a Rechester–Rosenbluth-type ansatz^{3,37} for CBC parameters, as was shown in Ref. 7. This model reads

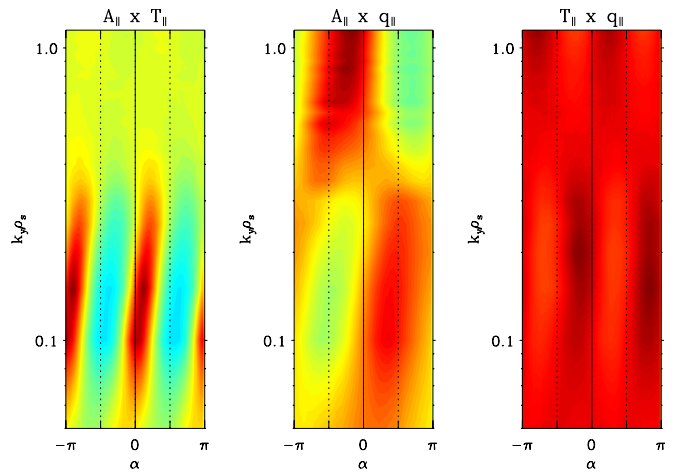


FIG. 17. (Color online) Nonlinear phases governing the magnetic transport. Plotted from left to right are the phases of the magnetic potential A_{\parallel} and the parallel temperature T_{\parallel} , the magnetic potential and the parallel heat conductivity q_{\parallel} , as well as T_{\parallel} and q_{\parallel} , corresponding to terms \mathcal{T}_2 , \mathcal{T}_3 , and \mathcal{T}_1 , respectively (see the text).

$$Q_e^{em} = \frac{\langle \tilde{q}_{e\parallel} \tilde{B}_x \rangle}{B_{ref}}, \quad (6)$$

$$\tilde{q}_{e\parallel} = -n_e \chi_{e\parallel} \left(\frac{d\tilde{T}_{e\parallel}}{dz} + \frac{\tilde{B}_x}{B_{ref}} \frac{d\tilde{T}_{e\parallel}}{dx} + \frac{\tilde{B}_x}{B_{ref}} \frac{dT_{e0}}{dx} \right), \quad (7)$$

where tildes indicate fluctuating quantities, \tilde{B}_x is the radial component of the magnetic field fluctuation, $\tilde{T}_{e\parallel}$ is the fluctuating part of the parallel electron temperature, and $\tilde{q}_{e\parallel}$ is the parallel electron heat conductivity. Three terms can be identified in the large brackets which – in order – shall be labeled \mathcal{T}_1 , \mathcal{T}_2 , and \mathcal{T}_3 , respectively. Together, they describe the parallel temperature gradient along the perturbed field lines. Note that in the case of linear simulations, the nonlinear term \mathcal{T}_2 drops out. One is left with the parallel diffusivity $\chi_{e\parallel}$. It is taken to be^{7,38}

$$\chi_{e\parallel} = q_0 R_0 \left(\frac{T_e}{m_e} \right)^{1/2}. \quad (8)$$

To gauge the applicability of the model to the TEM case, it is instructive to look at the phase relations governing the efficiency of the aforementioned terms. In linear simulations, the phase between $\tilde{T}_{e\parallel}$ and $\tilde{q}_{e\parallel}$ is $\sim -\pi/4$, while \tilde{B}_x and $\tilde{q}_{e\parallel}$ have a near-random phase relation, suggesting $\mathcal{T}_1 \gg \mathcal{T}_3$. As will be shown further below, $\tilde{B}_x \propto \beta$, and therefore one may predict the quasilinear transport ratio to scale as

$$\frac{Q_e^{em}}{Q_e^{es}} \propto \beta. \quad (9)$$

This scaling is found to predict the simulation behavior very well in both the CBC and the TEM case.

In Fig. 17, the nonlinear phase relations are shown. $\tilde{T}_{e\parallel}$ and $\tilde{q}_{e\parallel}$ have a random relative phase, while the phases obtained for the other two terms are similar, suggesting $\mathcal{T}_1 \ll \mathcal{T}_2 \sim \mathcal{T}_3$. However, the relative magnitudes of those terms are governed not only by their relative phases but also

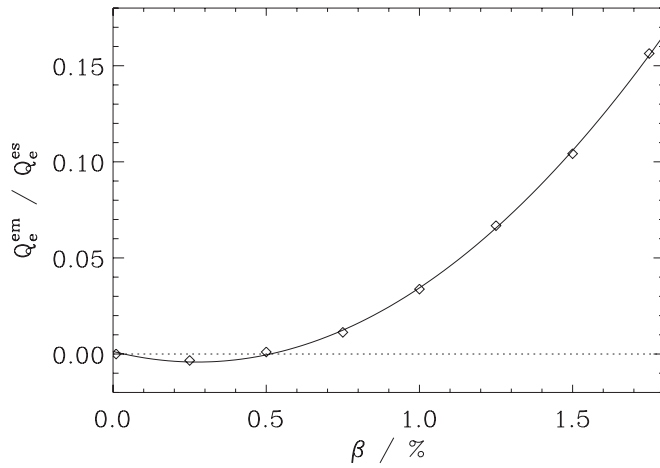


FIG. 18. Scaling of the nonlinear magnetic transport in the TEM case. The quadratic dependence on β reflects the results shown in Eq. (10).

by the amplitudes of their respective constituents. As becomes evident from Fig. 18, term T_3 must dominate in order to retain the quadratic scaling (much like in the CBC), and the resulting electron electromagnetic heat diffusivity reads

$$\chi_e^{\text{em}} = \eta_{\text{TEM}} q_0 R_0 \left(\frac{T_e}{m_e} \right)^{1/2} \frac{\langle \tilde{B}_x^2 \rangle}{B_{\text{ref}}^2}, \quad (10)$$

where η_{TEM} is a scaling factor of order unity which depends on the turbulence regime. Comparing the model to χ_e^{em} as obtained from the simulations directly, it is found that $\eta_{\text{TEM}} \sim 0.5$.

Note that for the ITG case presented in this work, the electromagnetic electron heat transport is negligible since in that scenario, the corresponding gradient is zero. Therefore, no evaluation of the magnetic transport model can be performed here.

VI. MAGNETIC FLUCTUATION STRENGTH

Particularly in the context of fast particle diffusion (e.g., the redistribution of beam ions in neutral beam injection heating scenarios³⁹), it is important to know the amplitude of the magnetic field perturbation, primarily its radial component. Expressions have been derived for the electrostatic and electromagnetic particle diffusivities in the case of both trapped and passing fast tracer particles,⁴⁰ and for the electromagnetic diffusivity of passing fast ions,

$$D_{\text{fi},p}^{\text{em}} \approx \left(\frac{R B_x}{\rho_s B_{\text{ref}}} \right)^2 \frac{\lambda_c}{6\eta^2}, \quad (11)$$

with the radial correlation length λ_c of the magnetic perturbations and the pitch angle η . In the same work, it was shown that these expressions are in excellent agreement with passive particle species behavior in the aforementioned CBC simulations. To compute the diffusivities quantitatively, a coefficient for the (linear) dependence of $B_x \equiv \tilde{B}_r$ on β is required, however, which may be obtained from a nonlinear β scan. For the CBC, it reads

TABLE I. Coefficients for the radial and toroidal magnetic field fluctuation amplitude, specified for different parameter cases. Within a single regime—i.e., ITG or TEM—only little change is observed.

Case	C_x	C_y
ITG	0.73	1.46
CBC: ITG	0.79	1.45
TEM	0.16	0.38
CBC: TEM	~ 0.4	~ 0.7

$$\frac{B_x}{B_{\text{ref}}} = \bar{C}_x \bar{\beta} \frac{\rho_s}{R_0} = C_x \frac{\beta}{\beta_{\text{crit}}} \frac{\rho_s}{R_0}, \quad \bar{C}_x = 0.6, \quad C_x = 0.79, \quad (12)$$

with $\bar{\beta} = 100\beta$. Note that the second formulation, which was used in Ref. 41, is somewhat more convenient in the present case, as its value does not change significantly within one instability regime, as can be inferred from Table I which lists the coefficients for all four cases: TEM, ITG, CBC: ITG regime, and CBC: TEM regime. Additionally, the respective coefficients for B_y/B_{ref} are provided. Since that value generally is more conveniently accessible, $\beta_{\text{crit}}^{\text{MHD}}$ was used for β_{crit} ; thus, should one aim to use the kinetic threshold instead, the ITG coefficients would be lowered slightly. In this form, it becomes clear that the fluctuation strength primarily depends on the turbulence type.

To obtain an indication how B_x depends on other physical quantities, simulations at a different temperature ratio were performed. $C_{x,y}$ should ideally be obtained from full β scans; however, certain trends may still be gathered from single β points. Decreasing the ion temperature to $T_i = 0.5$ leaves B_x unchanged (at $\mu = 40$) while increasing Q_i^{es} to 123, nearly twice the base value, as is to be expected. It may thus be tentatively concluded that B_x is independent of T_i . A more elaborate study would be required if one were to determine dependencies and obtain scaling exponents for all relevant physical parameters.

VII. CONCLUSIONS

In this paper, β scans of both TEM and ITG turbulence were presented to provide a basis for analyses of transport behavior and especially differences between linear expectations and the actual nonlinear results. For the TEM case, a slow decline of the linear growth rate with β was found to change to a moderate increase of the nonlinear transport. At the same time, the shearing rate was falling off with respect to the growth rate, indicating that a reduction in zonal flow strength was responsible for the transport β scaling, thereby explaining the discrepancy.

Linearly, the ITG growth rate was stabilized by an increasing β , up to the point where the mode became completely stable before the KBM threshold was reached. While qualitatively, this picture carried over to the nonlinear simulations, the decline occurred much faster. Again, zonal flows contribute to this behavior—the shearing rate decreases more slowly than the growth rate with β , thus inhibiting the transport. To quantify this effect, a study of the critical gradients

was performed. The linear ITG threshold experienced only small modifications throughout the entire β scan, while the nonlinear critical gradient increased rapidly, thus expanding the Dimits regime and stabilizing ITG turbulence over a wide range of β values. As changes to critical gradients are of great importance for experimental studies, this effect is one of the major findings of this work.

The impact of zonal flows in both scans seems to be fundamentally different. This, however, is the consequence of different linear growth rate behavior, while the shearing rate displays a rather similar decline in both cases. Another similarity is found in the good agreement of the linear and nonlinear KBM threshold. It is to be noted, however, that the kinetic β_{crit} is significantly smaller than the MHD ballooning threshold in the ITG case.

The Rechester–Rosenbluth-type model for magnetic transport was then successfully applied to the TEM case, corroborating its general applicability and hinting at its lack of sensitivity to unfavorable deviations in the phase relations. Like in the CBC, a quadratic scaling of the transport with β was obtained.

For both that model and the redistribution of fast particles in magnetic turbulence, the radial magnetic field fluctuation level B_x/B_{ref} is of great importance. It was found that by expressing that quantity in terms of the KBM threshold β_{crit} , it could be specified independently of the gradient choice within a single turbulence regime for the cases investigated here.

ACKNOWLEDGMENTS

The authors would like to thank S. Günter, T. Hauff, and W. M. Nevins for valuable discussions, and the Max Planck Society for funding the Interinstitutional Research Initiative “Turbulent transport and ion heating, reconnection, and electron acceleration in solar and fusion plasmas,” Project No. MIF-IF-A-AERO8047.

- ¹L. Vermare, F. Ryter, C. Angioni, A. G. Peeters, J. Stober, R. Bilato, L. D. Horton, B. Kurzan, C. F. Maggi, H. Meister, J. Schirmer, G. Tardini, and ASDEX Upgrade Team, *Nucl. Fusion* **47**, 490 (2007).
- ²D. C. McDonald, L. Laborde, J. C. DeBoo, F. Ryter, M. Brix, C. D. Challis, P. de Vries, C. Giroud, J. Hobirk, D. Howell, E. Joffrin, T. C. Luce, J. Mailloux, V. Pericoli-Ridolfini, A. C. C. Sips, K. Thomsen, and JET EFDA Contributors, *Plasma Phys. Controlled Fusion* **50**, 124013 (2008).
- ³F. Jenko and W. Dorland, *Plasma Phys. Controlled Fusion* **43**, A141 (2001).
- ⁴Y. Chen, S. E. Parker, B. I. Cohen, A. M. Dimits, W. M. Nevins, D. Shumaker, V. K. Decyk, and J. N. Leboeuf, *Nucl. Fusion* **43**, 1121 (2003).
- ⁵S. E. Parker, Y. Chen, W. Wan, B. I. Cohen, and W. M. Nevins, *Phys. Plasmas* **11**, 2594 (2004).

- ⁶J. Candy, *Phys. Plasmas* **12**, 072307 (2005).
- ⁷M. J. Pueschel, M. Kammerer, and F. Jenko, *Phys. Plasmas* **15**, 102310 (2008).
- ⁸B. D. Scott, *Phys. Plasmas* **7**, 1845 (2000).
- ⁹P. B. Snyder and G. W. Hammett, *Phys. Plasmas* **8**, 744 (2001).
- ¹⁰B. D. Scott, *Plasma Phys. Controlled Fusion* **45**, A385 (2003).
- ¹¹B. D. Scott, *Plasma Phys. Controlled Fusion* **48**, B277 (2006).
- ¹²M. J. Pueschel, L. Laborde, and F. Jenko, Proceedings of the 35th EPS Conference on Plasma Physics, Hersonissos, 2008, Vol. 32D, p. 1.038.
- ¹³M. Kotschenreuther, W. Dorland, M. A. Beer, and G. W. Hammett, *Phys. Plasmas* **2**, 2381 (1995).
- ¹⁴F. Jenko, T. Dannert, and C. Angioni, *Plasma Phys. Controlled Fusion* **47**, B195 (2005).
- ¹⁵A. M. Dimits, G. Bateman, M. A. Beer, B. I. Cohen, W. Dorland, G. W. Hammett, C. Kim, J. E. Kinsey, M. Kotschenreuther, A. H. Kritiz, L. L. Lao, J. Mandrekas, W. M. Nevins, S. E. Parker, A. J. Redd, D. E. Shumaker, R. Sydora, and J. Weiland, *Phys. Plasmas* **7**, 969 (2000).
- ¹⁶F. Jenko, W. Dorland, M. Kotschenreuther, and B. N. Rogers, *Phys. Plasmas* **7**, 1904 (2000).
- ¹⁷T. Dannert and F. Jenko, *Phys. Plasmas* **12**, 072309 (2005).
- ¹⁸F. Merz, Ph.D. thesis, University of Münster, 2008.
- ¹⁹M. J. Pueschel, T. Dannert, and F. Jenko, *Comput. Phys. Commun.* **181**, 1428 (2010).
- ²⁰See: <http://www.ipp.mpg.de/~fsj/gene> for information on/access to the GENE code.
- ²¹M. Kammerer, F. Merz, and F. Jenko, *Phys. Plasmas* **15**, 052102 (2008).
- ²²P. Xanthopoulos and F. Jenko, *Phys. Plasmas* **13**, 092301 (2006).
- ²³F. Merz and F. Jenko, *Phys. Rev. Lett.* **100**, 035005 (2008).
- ²⁴J. Lang, S. E. Parker, and Y. Chen, *Phys. Plasmas* **15**, 055907 (2008).
- ²⁵D. R. Ernst, J. Lang, W. M. Nevins, M. Hoffman, Y. Chen, W. Dorland, and S. Parker, *Phys. Plasmas* **16**, 055906 (2009).
- ²⁶D. R. Ernst, P. T. Bonoli, P. J. Catto, W. Dorland, C. L. Fiore, R. S. Granetz, M. Greenwald, A. E. Hubbard, M. Porkolab, M. H. Redi, J. E. Rice, K. Zhurovich, and Alcator C-Mod Group, *Phys. Plasmas* **11**, 2637 (2004).
- ²⁷M. J. Pueschel, Ph.D. thesis, University of Münster, 2009.
- ²⁸J. Wesson, *Tokamaks* (Clarendon, Oxford, 1997).
- ²⁹T. S. Hahm, M. A. Beer, Z. Lin, G. W. Hammett, W. W. Lee, and W. M. Tang, *Phys. Plasmas* **6**, 922 (1999).
- ³⁰P. Xanthopoulos, F. Merz, T. Görler, and F. Jenko, *Phys. Rev. Lett.* **99**, 035002 (2007).
- ³¹F. Zonca, L. Chen, J. Q. Dong, and R. A. Santoro, *Phys. Plasmas* **6**, 1917 (1999).
- ³²P. H. Diamond, S.-I. Itoh, K. Itoh, and T. S. Hahm, *Plasma Phys. Controlled Fusion* **47**, R35 (2005).
- ³³V. Naulin, A. Kendl, O. E. Garcia, A. H. Nielsen, and J. Juul Rasmussen, *Phys. Plasmas* **12**, 052515 (2005).
- ³⁴B. D. Scott, *New J. Phys.* **7**, 92 (2005).
- ³⁵W. M. Nevins, E. Wang, I. Joseph, J. Candy, S. E. Parker, Y. Chen, and G. Rewoldt, *Bull. Am. Phys. Soc.* **54**, 15 (2009).
- ³⁶D. R. Mikkelsen and W. Dorland, *Phys. Rev. Lett.* **101**, 135003 (2008).
- ³⁷A. B. Rechester and M. N. Rosenbluth, *Phys. Rev. Lett.* **40**, 38 (1978).
- ³⁸Z. Chang and J. D. Callen, *Phys. Fluids B* **4**, 1167 (1992).
- ³⁹S. Günter, G. Conway, S. daGraça, H.-U. Fahrbach, C. Forest, M. Garcia Muñoz, T. Hauff, J. Hobirk, V. Igochine, F. Jenko, K. Lackner, P. Lauber, P. McCarthy, M. Maraschek, P. Martin, E. Poli, K. Sassenberg, E. Strumberger, G. Tardini, E. Wolfrum, H. Zohm, and ASDEX Upgrade Team, *Nucl. Fusion* **47**, 920 (2007).
- ⁴⁰T. Hauff, M. J. Pueschel, T. Dannert, and F. Jenko, *Phys. Rev. Lett.* **102**, 075004 (2009).
- ⁴¹R. E. Waltz, *Phys. Fluids* **28**, 577 (1985).